Acute influenza infection promotes lung tumor growth by reprogramming the tumor microenvironment

Irati Garmendia, Aditi Varthaman, Solenne Marmier, Mahmud Angrini, Ingrid Matchoua, Aurelie Darbois-Delahousse, Nathalie Josseaume, Pierre-Emmanuel Foy, Lubka T. Roumenina, Naïra Naouar, et al.

Acute influenza infection promotes lung tumor growth by reprogramming the tumor microenvironment

Irati Garmendia[1#], Aditi Varthaman[1#], Solenne Marmier[1#], Mahmud Angrini[1], Ingrid Matchoua[1], Aurelie Darbois-Delahousse[2], Nathalie Josseaume[1], Pierre-Emmanuel Foy[1], Lubka T. Roumenina[1], Naïra Naouar[3], Maxime Meylan[1], Sophie Siberil[1], Jules Russick[1], Pierre-Emmanuel Joubert[1], Karen Leroy[1,4], Diane Damotte[1,5], Audrey Mansuet-Lupo[1,5], Marie Wislez[1,6], Marco Alifano[1,7], Laurie Menger[2], Ignacio Garcia-Verdugo[8], Jean-Michel Sallenave[8], Olivier Lantz[2,9,10], Florent Petitprez[11,12], and Isabelle Cremer[1*].

co-first authors

Affiliations

1. Centre de Recherche des Cordeliers, Sorbonne Universite, Inserm, Universite Paris Cite, Team Inflammation, complement and cancer, F-75006, Paris, France.

2. INSERM U932, PSL Universite, Institut Curie, Paris, F-75005, France.

3. ARTbio platform, Institut de Biologie Paris Seine, Sorbonne-Universite, F-75252, Paris, France. Institut français de bioinformatique.

4. Department of biochemistry, hopital Europeen Georges Pompidou, Assistance Publique Hopitaux de Paris Centre ; Universite Paris Cite, F-75015, Paris, France

5. Departments of pathology and thoracic surgery, hopital Cochin, Assistance Publique Hopitaux de Paris Centre, Universite Paris Cite F-75014, Paris, France.

6. Department of respiratory medicine and thoracic oncology, hopital Cochin, Assistance Publique Hopitaux de Paris Centre, Universite Paris Cite, F-75014, Paris, France.

7. Department of thoracic surgery, hopital Cochin, Assistance Publique Hopitaux de Paris Centre, Universite Paris Cite, F-75014, Paris, France.

8. INSERM U1152, laboratoire d'Excellence Inflamex, Universite Paris Cite, Hopital Bichat - Claude-Bernard, Paris, F-75018, France.

9. Laboratoire d'immunologie clinique, Institut Curie, Paris, F-75005, France.

10. Centre d'investigation clinique en biotherapie, Institut Curie (CIC-BT1428), Paris, F-75005, France.

11. Programme cartes d'identite des tumeurs, ligue nationale contre le cancer, F-75013, Paris, France.

12. MRC Centre for Reproductive Health, Queen's Medical Research Institute, The University of Edinburgh, Edinburgh EH16 4TJ, UK.

*** Corresponding author:**

Dr. Isabelle Cremer

Cordeliers Research Center, INSERM UMRS 1138

15 rue de l'Ecole de Medecine; 75006 Paris, France

e-mail: isabelle.cremer@sorbonne-universite.fr

ORCID : 0000-0002-0963-1031

Conflict-of-interest statement: The authors declare no potential conflicts of interest.

Funding Information: This work was supported by the "Institut National de la Sante et de la Recherche Medicale" (INSERM), Sorbonne Universite, Universite Paris Cite, the LabEx Immuno-Oncology, the Institut National du Cancer (2016-PLBIO) and foundation ARC.

Running Title: Pro-tumoral effects of influenza infection in lung carcinoma

Keywords: non-small cell lung cancers, influenza virus, immune exhaustion, immunosuppression, drug metabolism

Synopsis: The authors show in lung-cancer models that acute influenza virus infection has a long-term effect on the tumor microenvironment impacting antitumor immune responses, tumor progression and survival, with implications for prophylactic and therapeutic management of lung cancer patients.

.

Abstract

One billion people worldwide get flu every year, including patients with non-small cell lung cancer (NSCLC). However, the impact of acute influenza A virus (IAV) infection on the composition of the tumor microenvironment (TME) and the clinical outcome of patients with NSCLC is largely unknown. We set out to understand how IAV load impacts cancer growth and modifies cellular and molecular players in the TME. Herein, we report that IAV can infect both tumor and immune cells, resulting in a long-term pro-tumoral effect in tumor-bearing mice. Mechanistically, IAV impaired tumor-specific T-cell responses, led to the exhaustion of memory $CD8^+$ T cells and induced PD-L1 expression on tumor cells. IAV infection modulated the transcriptomic profile of the TME, fine-tuning it towards immunosuppression, carcinogenesis, and lipid and drug metabolism. Consistent with these data, the transcriptional module induced by IAV infection in tumor cells in tumor-bearing mice was also found in human lung adenocarcinoma patients and correlated with poor overall survival. In conclusion, we found that IAV infection worsened lung tumor progression by reprogramming the TME towards a more aggressive state.

Introduction

The tumor microenvironment (TME) is a complex ecosystem comprising tumor cells, fibroblasts, endothelial and immune cells which strongly influences clinical outcome and response to treatments (1–3). In the past decade, the central role of the lung TME in tumor control or progression has been underlined (4,5). In non-small cell lung cancer (NSCLC), the most common subtype of lung cancer, the study of the immune landscape shows robust infiltration of T lymphocytes co-expressing immune checkpoints, B lymphocytes, NK cells, macrophages and neutrophils (5–9). In addition, the TME is highly heterogeneous between patients, but how the individual TME is shaped and evolves during tumor progression is not completely understood. Several factors influence the TME, such as specific tumor mutations and tumor mutational burden (10,11), epigenetic modifications (12), tumor cell metabolism (13), chronic inflammation, such as in the context of chronic obstructive pulmonary disease (COPD), and the lung microbiome (14–17). However, the effect of acute respiratory viral infections has barely been investigated so far. NSCLC patients may experience influenza A virus (IAV) infection during the course of their cancer, but the impact of acute IAV on lung tumor progression and antitumor immune responses is largely unexplored.

IAV infection occurs worldwide in a seasonal cycle. It causes acute respiratory disease and results in 3 to 5 million cases of severe illness (18). Elderly and immunocompromised individuals, such as those with lung cancer, are more likely to be infected and to develop severe respiratory disorders (19–21). Among the potential mechanisms, IAV is a single-stranded RNA (ssRNA) virus that infects airways epithelial cells and is intracellularly recognized by RNA sensors, notably toll-like receptor 7 (TLR7) (22). We have previously shown that TLR7 is highly expressed by malignant cells in patients with NSCLC and confers a poor clinical outcome (23). Stimulation of tumor cells with TLR7 synthetic agonists induces NF-κB activation and Bcl-2 expression, increased tumor progression and resistance to chemotherapy in murine tumor models (24,25). In this study, we sought to analyze the impact of IAV infection on the long-term progression of NSCLC using subcutaneous, orthotopic and genetically induced tumor models. We found that acute IAV infection of lung tumor–bearing mice increased tumor progression,

induced tumor nodules of a higher grade and favored immunosuppression. RNA sequencing of the tumor-bearing lungs from non-infected and IAV-infected mice revealed a distinct transcriptomic profile suggesting a specific TME induced by viral infection. Finally, we show that in patients, expression of this signature in epithelial cells predicted poor overall survival in the lung adenocarcinoma (LUAD) subtype of NSCLC.

Material and Methods

Cell lines

KP cells (lung adenocarcinoma subtype expressing luciferase), derived from tumor-bearing lungs of *Kras*$^{LSL\text{-}G12D/+}$*Trp53*$^{flox/flox}$ mice, were kindly provided by Dr. Laurie Menger (Institut Curie, Paris). KP cells were cultured in RPMI 1640 medium (Gibco, cat# 61870) supplemented with 10% heat-inactivated FCS (Eurobio, cat# CVFSVF00-01) and 1% penicilin/streptomycin (Gibco, cat# 15140) (the cells were not cultured more than passage 15). LLC cells (Lewis Lung Carcinoma, ATCC CRL-1642; gift from Vincenzo di Bartolo in 2015, Institut Pasteur, Paris) were stably transfected with firefly luciferase. LLC cells were cultured in DMEM + Glutamax (Gibco, cat# 61965) with 10% heat-inactivated FCS, 1% penicillin/streptomycin and 1% hygromycin B (Thermo Scientific Chemicals, cat# J60681) (the cells were not cultured more than passage 15). All cell lines were routinely tested for Mycoplasma with a kit (Ozyme, cat# LT07-710) and used only if negative. No specific authentication of the cell lines was performed.

Tumor induction in mice

Subcutaneous tumor models: B6(C)/Rj-Tyr$^{c/c}$ mice (Janvier Labs) were subcutaneously injected with 10^5 KP cells or $2x10^4$ LLC cells in their right flanks. Tumor progression was measured every 2–3 days by bioluminescence using IVIS Lumina II *In vivo* Imaging System (Perkin Elmer) for KP cells and by caliper for LLC cells. To measure tumors from KP cells, mice were injected intraperitoneally with D-Luciferin (XenoLight D-Luciferin-K$^+$ Salt, PerkinElmer, cat# 122799; 150 mg Luciferin/kg body weight). Ten minutes after D-Luciferin injection, the bioluminescent signal was acquired during 5 min using the IVIS Lumina II system (Perkin Elmer, Waltham, MA, USA). During the acquisition procedure, mice were anesthetized with 2.5% isoflurane (XGI-8 Gas anesthesia system, Perkin Elmer) for 10 min. Data were analyzed with Living image software by defining a region of interest on the thoracic area of each mouse and extracting the corresponding total flux. For LLC cells, tumor growth was monitored via repeated measurements of the tumor size using a digital caliper. Tumor volume was calculated using the following formula: tumor size (mm^3) = (length × width × height)/8 × 4/3 × π.

Orthotopic tumor model: B6(C)/Rj-Tyr$^{c/c}$ mice were intravenously injected with 5x10^4 KP cells in their tail vein. Tumor progression was measured weekly by measuring bioluminescence. We choose to use B6(C)/Rj-Tyr$^{c/c}$ mice because, being albinos, they are more suitable for IVIS imaging.

Transgenic mice: Lung adenocarcinoma were induced in 8–12 weeks-old female *Kras*$^{LSL\text{-}G12D/+}$*Trp53*$^{flox/flox}$ mice (referred to as KP mice, kindly provided by Dr. Tyler Jacks, Massachusetts Institute of Technology, Cambridge, MA) by intratracheal administration of 2x10^4 lentiviral (LTV) particles as previously described (26). Lentivirus was generated from Cre recombinase-expressing plasmids in Dr. Olivier Lantz's laboratory to express the MHC class I OVA epitopes fused to the C-terminal end of the luciferase protein (27). *In vivo* tumor progression was measured weekly by measuring bioluminescence using IVIS Lumina II *In vivo* Imaging System (Perkin Elmer).

All mice were housed in specific pathogen free (SPF) conditions in full accordance with FELASA recommendations. All procedures were performed in compliance with European Union Directive 63/2010 and received approval from the Charles Darwin Ethics Committee for animal experimentation. (APAFIS 18589 - 201901211717868).

IAV infection of tumor-bearing mice

For the subcutaneous lung tumor models, when tumors were appreciable (10–13 days post-cells injection), mice were randomly divided into the different groups: the groups of IAV-infected mice were intratumorally infected either with the Influenza A/Scotland/20/74 (H3N2 strain) virus or the A/PR/8/34 (H1N1 strain) (150 or 1000 pfu in 100 µL PBS). Non-infected control mice were injected with PBS.

For the orthotopic lung tumor model, when tumors were detectable (total flux around 1x10^5 photon/s), mice were randomly divided into two groups, one intranasally infected with H3N2 IAV (150 pfu in 40 µL PBS) and the other one with PBS.

For the genetic lung tumor model, eleven weeks after lentiviral inoculation, KP mice were infected with H3N2 IAV by intranasal inoculation (150 pfu in 40 µL PBS). Control mice received PBS alone. IAV

infection was confirmed by measuring the body weight loss of the mice daily after viral infection and quantifying anti-IAV immunoglobulins. Mice were euthanized 16 weeks after lentiviral delivery.

Both IAV strains, originally obtained from Professor S. Van der Werf (Institut Pasteur, Paris) were purified as previously described (28). Tumor growth was followed up by IVIS Lumina II *In vivo* Imaging System (Perkin Elmer).

Immunohistochemistry

Mice were perfused intracardially with PBS followed by 4% paraformaldehyde (Chem Cruz, cat# sc-281692) at room temperature before dissection. Lung tissue was embedded in paraffin using a Leica ASP300/Histocore Arcadia H instrument. Histological 3–5 µm sections were processed by cutting 20 slides to perform hematoxylin (Dako, cat# 53309) and eosin (Abcam, cat# ab246824) (HE) staining. Three slides for each were used for the quantification (using the first slide, the 10^{th} and the 20^{th}). All slides were scanned with the NanoZoomer 2.0HT (Hamamatsu manufacturer) and analyzed by NDP.view2 viewing software (Hamamatsu manufacturer). We counted the number of tumor nodes and identified the grade of the tumors in HE sections, based on the tissue histology, as previously described (26) and with the help of a pathologist, who validated our quantification. Finally, the surface area of the tumor and the tissue were quantified with NDP.view2 viewing software (Hamamatsu manufacturer).

For immunofluorescence staining of murine and human tumors (see below), antigen retrieval was done at 97 °C for 30 min at pH 9 using a PT-Link instrument (Dako). Primary antibody staining was carried out for 15 min at RT, followed by the use of polymers for 10 min at RT. Antibody detection was performed with Opal technology. A list of the antibodies and other reagents used in the immunofluorescence staining can be found in **Supplementary Table S1**. All sections were stained with DAPI (1 µg/mL, Invitrogen, cat# D21490) for 5 min and mounted in Prolong Diamond antifade mounting (Invitrogen, cat# P36961). Slides were scanned using Axioscan (Zeiss) and the analysis and quantification were done with Halo software version 3.5 (Indica Labs).

Anti-influenza antibody quantification by ELISA

Blood collected from anesthetized mice was centrifuged at 10,000 rpm for 10 min at 4 °C. Purified IAV was coated at 1 x 6 pfu/mL overnight at 4 °C in 96 microtiter plates (Greiner). After washing, blocking was performed with 2% BSA and 0.05% Tween-20 in PBS for 2 hours at RT. Serial dilutions of plasma were prepared in 0.1% BSA, 0.05% Tween and PBS buffer, and incubated for 1.5 hours at 37°C. Mouse HRP-conjugated IgG (Southern Biotech, cat# 1030-05) or mouse HRP-conjugated IgM (Millipore, cat# AP500P) diluted at 1:10,000 were used as detection antibodies for 30 min at 37°C. Peroxidase activity was revealed using sigmaFAST OPD (Sigma, cat# P9187). The colorimetric reaction was stopped using H_2SO_4 and plates were read at 492 nm on the SPARK 10M reader (Tecan). IgG and IgM concentrations were determined using a standard curve of mouse purified total IgG (Sigma, cat# PP54) or IgM (Sigma, cat# PP50).

Flow cytometry of *in vitro* IAV-infected KP cells

In vitro IAV-treated (KP cells: 0.01 or 0.05 MOI for 24, 48 and 72 hours; LLC cells: 1 or 2 MOI for 24, 48 and 72 hours) and non-treated cells were detached using trypsin (Gibco, cat# 25300-054) and washed in RPMI 1640 10% heat-inactivated FCS (complete medium). Fc receptors were blocked using purified anti-mouse CD16/CD32 (1:50, BD Pharmingen). Cells were stained with LIVE/DEAD™ Fixable Yellow dead cell staining kit (1:100, Invitrogen, cat# L32250), anti-PD-L1 and anti-MHC class-I (H-2Kb) (information regarding the antibodies can be found in **Supplementary Table S2**). Cells were washed, fixed and permeabilized using the intracellular fixation and permeabilization buffer set (eBioscience, cat# 88-8823-88), according to the manufacturer's guidelines. Intracellular staining was performed using an anti-influenza A virus nucleoprotein (NP) (**Supplementary Table S2**). Cells were analyzed using a BD Fortessa X20 flow cytometer (BD Biosciences). Data was studied using Kaluza Analysis software, version 1.3 (Beckman Coulter).

Flow cytometry analyses of lungs from KP mice

Mouse lungs were harvested in RPMI 1640 medium (Gibco) into gentleMacs C tubes (Miltenyi) and enzymatically digested with the Miltenyi tumor dissociation kit (cat# 130-096-730) by using the

gentleMACS™ octo dissociator at 37°C, according to manufacturer's instructions. Tumor adjacent normal tissue was excluded at maximum so that only tumor tissue was included in these analyses. Tumor-bearing lung pieces were manually filtered through a 70 µm cell strainer. Erythrocytes were lysed in ACK buffer for 5 min and the reaction was halted with RPMI 1640 medium. Approximately 2 million cells were transferred into a 96-well plate for flow cytometry staining. Fc receptors were blocked with anti-mouse CD16/CD32 (1:100, BD Pharmingen) along with Zombie™ Aqua Fixable Viability dye (BioLegend) for 10 min at RT. Cells were washed with PBS followed with specific antibody staining diluted in PBS for 15 min at RT. All antibodies used are listed in **Supplementary Table S2**. Mouse MHC class I tetramers (H-2K(b) chicken OVA 257-264 SIINFEKL-PE tetramer and H-2D(b) Influenza A PA (polymerase acidic protein) 224-233 SSLENFRAYV-BV421 tetramer) were kindly provided by the NIH Tetramer Core Facility. Tetramer staining was performed in PBS at RT for 15 min prior to staining of cell surface proteins. The anti-CD8 clone KT15 (at 1:200 dilution) was used in concert with tetramer staining to avoid antibody competition with the CD8 molecule for MHC class I molecule binding. After staining, cells were resuspended in PBS 4% paraformaldehyde for 10 min, washed twice in PBS and analyzed using a BD Fortessa X20 flow cytometer (BD Biosciences). Absolute cell counts were determined by using CountBright Absolute Counting Beads (Invitrogen, cat# C36950) following the manufacturer's recommendations. Results were plotted and analyzed using the FlowJo 10 software.

Unsupervised analysis of the flow cytometry data was performed using RStudio software 1.3.959 and the Excyted pipeline (https://github.com/maximemeylan/Excyted) (29). T cells and NK and B cells panels were analyzed by the unsupervised strategy. Intensity values of events gated from live cells were normalized with the Logicle transformation. Uniform Manifold Approximation and Projection (Umap) calculation and unsupervised clustering was performed with 10,000 events for each sample using k=30 and Rphenograph (Leland McInnes arXiv:1802.03426, https://github.com/i-cyto/Rphenograph). Further re-clustering in the T cells panel was carried out by re-running the Excyted pipeline on selected CD3-positive clusters using k=100.

Taqman assay for viral sensors and Interferon-Stimulated Genes

RNA was extracted using the RNeasy Mini Kit (Qiagen, cat# 74136) from KP cells infected with 0.01 or 0.05 MOI of IAV for 24, 48 and 72 hours. Non-infected cells were used as control. The quality and quantity of extracted RNA were tested by using Agilent RNA 6000 Nano Kit (Agilent Technologies cat# 5067-1511) and Agilent Bioanalyzer according to the manufacturers' guidelines. Reverse transcription of RNA to cDNA was performed using 1 µg of total RNA using high-capacity cDNA Reverse transcription kit (Applied Biosystems, cat# 10400745) and Thermocycler Eppendorf nexus Mastercycler. For individual gene expression analysis, qPCR reactions were carried out by using FastStart Universal Probe Master Mix (Roche, cat# 4913949001) and inventoried TaqMan probes (FAM-MGB dye) specific for murine *Tlr7* (Thermofisher Scientific, cat# Mm00446590_m1), *Tlr3* (Thermofisher Scientific, cat# Mm01207404_m1), *Ddx58* (Thermofisher Scientific, cat# Mm01216852_m1), *Ifih1* (Thermofisher Scientific, cat# Mm00459183_m1) and *Gapdh* (Thermofisher Scientific, cat# Mm99999915_g1), according to manufacturer guidelines. These experiments were performed in triplicates. Gene expression was determined by fold-change ($2^{-\Delta\Delta Ct}$) comparing infected and non-infected samples.

TaqMan® gene expression array was performed using the TaqMan Array Mouse Immune Panel (Applied Biosystems, cat# 4367786) following recommendations of the manufacturer, for the study of interferon-stimulated genes' (ISGs) expression. The plates were read on a 7900HT Fast Real-Time PCR System (Thermofisher).

Bulk RNA sequencing

Primary human lung tumors were obtained after resection surgery at Cochin Hospital (Paris). Written informed consent was obtained from the eight patients before participation. The patients included in this study signed an informed consent form prior to inclusion. The research was approved (CPP Ile-de-France II n°2012-06-12) by the medical ethics board at Cochin Hospital and conducted according to the recommendations in the Helsinki Declaration. Tumors were cut in two pieces of approximately 5 mm^3: one part was infected with IAV (closed to MOI 1) for 24 hours, while the other part was not infected and served as control.

Total RNA was extracted from human tumors and tumor-bearing lungs from mice infected or not with IAV. RNA was extracted using the Maxwell 16 LEV simply RNA tissue kit (Promega, cat# AS120) and was quantified using the fluorometric qubit RNA assay (Life Technologies, cat# Q32852). RNA integrity (RIN) was determined with the Agilent 2100 bioanalyzer (Agilent Technologies). RNA sequencing was performed at the GENOM'IC platform (Cochin Institute, Paris). To construct the libraries, 1 µg of high-quality total RNA (RIN ≥ 8 for murine tumors, RIN ≥ 5 for human tumors) was processed using TruSeq Stranded mRNA kit (Illumina, cat# 20020594). Briefly, after purification of poly-A containing mRNA molecules, these were fragmented and reverse-transcribed using random primers. Replacement of dTTP by dUTP during the second strand synthesis permitted high strand specificity. Addition of a single A base to the cDNA was followed by ligation of Illumina adapters. Libraries were quantified by qPCR using the KAPA library quantification kit for Illumina libraries (Kapa Biosystems, cat# 5067-4626) and library profiles were assessed with the DNA high sensitivity labchip kit on an Agilent bioanalyzer. Libraries were sequenced on an Illumina NextSeq 500 system using 75 base-lengths read V2 chemistry in a paired-end mode. After sequencing, a primary analysis based on AOZAN software (ENS, Paris) was applied to demultiplex and control the quality of the raw data (based on FastQC modules, version 0.11.5).

Statistical and bioinformatics analyses

Comparisons of tumor growth were analyzed by using the two-way ANOVA with Sidak correction for multiple comparisons. Correlation between IAV infection and the expression of viral sensors, PD-L1 and MHC-I was calculated by Spearman correlation. Differences in cytokine expression between IAV-infected and non-infected KP cells were studied by linear regression with Benjamini-Hochberg correction for multiple testing. The percentage of tumor nodules with different grades per total lung lobule were compared between groups with the Chi-Squared test. Data obtained from immunofluorescent staining were compared with the Mann-Whitney *U* test. Differences in IgM and IgG anti-IAV were studied with the ordinary one-way ANOVA with Sidak correction for multiple comparisons. Data obtained from flow cytometry and studied by the supervised gating strategy were

analyzed by multiple Mann-Whitney tests with Benjamini-Hochberg correction, except for data concerning Tregs, B cells activation and myeloid subsets (1-way ANOVA) as well as PD-1 expression in OVA-tetramer$^+$ as compared to IAV-tetramer$^+$ CD8$^+$ T cells (Mann-Whitney *U* test). Differences in clusters found by the unsupervised analysis of flow cytometry data were studied by the Mann-Whitney *U* test. All these statistical analyses were performed using GraphPad Prism software (version 9.2.0).

Differential gene expression analysis from RNA-Seq data (mouse and human tumors) was performed using Galaxy Software (ARTBio platform, IBPS, Paris). Fastq files obtained were aligned using the HiSAT2 algorithm (on MM10 murine and on GRCH38 human reference genomes) and quality control of the alignment was performed with the RSeQC package. Reads were counted using htseq-count and the analysis of differential expression was performed with the DESeq2 package and Biomart (mouse GRC38p6). KEGG and GO Biological processes were interrogated and GSEA analysis was done using the R package GSEABase. These analyses were performed using R version 4.1.3.

TCGA LUAD analysis

For TCGA analysis, gene expression and clinical data from the TCGA LUAD cohort (30) were obtained from the Genomics Data Portal (https://portal.gdc.cancer.gov) for n=473 tumors. FPKM data were normalized and set to logarithmic scale. For the REVISE signature definition, human orthologs of genes overexpressed in infected compared to non-infected mice were obtained using the R package biomaRt. The Pearson correlation matrix of the expression of these genes in the TCGA LUAD cohort was examined and clustered using hierarchical clustering with Euclidian distance and Ward criterion. Five groups were identified from the clustering, each with strong intra-group correlation and low correlation between groups. These groups were labeled 1 to 5. The impact on survival was estimated using Kaplan-Meier curves and logrank test.

In all statistical studies, *: $P < 0.05$, **: $P < 0.01$, ***: $P < 0.001$ and ****: $P < 0.0001$.

OncoSg analysis

For oncoSg analysis, gene expression (log RNA-seq V2 RSEM) and clinical data (31) were obtained from cBioPortal (https://www.cbioportal.org) for n=169 samples. The impact on survival was estimated using Kaplan-Meier curves and logrank test with the R package survival.

GSE131907 single-cell RNA-seq analysis

For Single-cell RNA-sequencing analysis, gene expression (log_2 TPM) and metadata from cohort GSE131907 (32) were downloaded from the Gene Expression Omnibus portal. Only cells from lung tumor samples (Sample_Origin "tLung", n = 11 samples) were kept. Data visualization and analysis was performed using the R package Seurat v4 (33).

COPD cohort analysis

Data was obtained from cohort GSE124180 (34) Gene counts and metadata were downloaded from the Gene Expression Omnibus portal and transformed into TPM values. Data visualization and analysis was performed using R.

Data availability statement

The data generated in this study are available at the European Nucleotide Archive (ENA) study, accession number: PRJEB59490 or from the corresponding author upon reasonable request.

Results

IAV infection enhances tumor growth in subcutaneous, orthotopic and genetically-induced autochthonous lung adenocarcinoma

In an attempt to characterize the molecular modifications induced after IAV infection, KP and LLC cells were *in vitro* infected (H3N2 strain). We observed productive infection as revealed by viral nucleoprotein (NP) expression, which increased between 24 and 72h after infection **(Fig.1A, Supplementary Figure 1A,B)**, concomitant with upregulation of the viral sensors Interferon Induced With Helicase C Domain 1 (Ifih1), TLR3, TLR7 and DExD/H-box helicase 58 (Ddx58), in addition to CD274 and MHC-I (**Fig. 1A**)**.** We also found that many genes encoding molecules involved in immune response regulation including the cytokines IL-1α, TNF-α, IL-6 and IL-13, the chemokines CXCL10 and CXCL11, and Nos2 or HMOX1 were highly increased by IAV in tumor cells, suggesting that IAV may influence the TME composition (**Fig. 1B**). Additionally, IAV infection did not alter cell viability of LLC cells and reduced KP cell viability by 40% 72h after infection **(Supplementary Fig. S1A,B)**.

We analyzed the effect of IAV infection in subcutaneous and orthotopic murine models of lung carcinoma cells injection. KP and LLC cells were first subcutaneously injected in B6(C)/Rj-Tyrc/c mice and intratumoral IAV infection (150 and 1000 pfu/mice) was performed. Increased tumor growth was induced by IAV infection as compared to non-infected subcutaneous tumors both in the KP (**Fig. 1C-D**) and in the LLC tumor model, whatever the strain of IAV and the dose of virus injected (**Supplementary Fig. S2**). For the orthotopic model, KP cells were inoculated in mice by intravenous injection. As soon as lung tumors were detected around 13 days post-cells injection, mice were intranasally infected with IAV (150 pfu/mice). Again, IAV infection significantly increased the growth of already established tumors (**Fig. 1E-F**).

We then studied the effect of intranasal IAV infection on lung tumor progression in a mouse model of genetically-induced autochthonous lung adenocarcinoma (LUAD, the most common histologic subtype of NSCLC) driven by the expression of oncogenic *Kras*^{G12D} and loss of *p53* (*Kras*$^{LSL\text{-}G12D/+}$*Trp53*$^{flox/flox}$, KP mice) (26). Tumor progression was monitored weekly by bioluminescence imaging and when 50% of

mice developed detectable tumors (total flux <2x10^5 photon/s, week 11 post-LTV inoculation), mice were intranasally administered with a sublethal dose of IAV or PBS (experimental design in **Fig. 2A**). Non-LTV-inoculated mice, all of which did not develop tumors, served as controls. IAV infection in tumor-bearing mice resulted in significantly larger tumors at 5 weeks post-infection (**Fig. 2B-C**) and reduced survival **(Fig. 2D)** as compared to non-infected tumor-bearing mice. IAV infection resulted in a comparable reduced body weight in all infected mice with or without tumors (loss of 15–20%, 10 days after infection) (**Fig. 2E**). Furthermore, both control and tumor-bearing mice had detectable anti-IAV IgM and IgG titers in the serum following viral infection when sacrificed (**Fig. 2F**), which further confirmed that all mice were successfully infected. Histological characterization of the lung tumors (performed as in (26)) revealed higher tumor grade in IAV-infected lungs compared to the non-infected ones (**Fig. 2G**). Viral hemagglutinin (HA) protein was detected in both epithelial pan cytokeratin (panCK$^+$) tumor cells (median of 4.6% HA$^+$ cells) and CD45$^+$ immune cells (median of 2.2% HA$^+$ cells) (**Fig. 2H-I**), showing that IAV infects both tumor and immune cells and persists long term in the lungs (up to 5 weeks after infection). In addition, viral infection induced high PD-L1 expression in panCK$^+$ malignant cells (from 2.8% to 32%, P=0.009) (**Fig. 2J-K**), consistent with the *in vitro* upregulation of PD-L1 after IAV infection in KP cells (**Fig. 1A**).

These results demonstrate that acute IAV infection of tumor and immune cells in the TME accelerates lung tumor growth.

Influenza A virus infection affects tumor-associated CD8$^+$ T cells

To understand the underlying causes of the accelerated tumor growth upon IAV infection, we performed a comprehensive immune cell phenotyping analysis of the lungs of tumor-bearing and non-tumor-bearing KP mice by flow cytometry, at sacrifice (**Supplementary Fig. S3A-D** describes the gating strategies). Although the distributions of CD4$^+$ and CD8$^+$ T cells, NK cells, B cells and myeloid cells were similar between the groups (**Supplementary Fig. S4A**), the T-cell compartment was markedly affected by IAV infection. In particular, IAV infection led to an increase in effector and effector memory CD8$^+$ T-cell populations in lungs both with and without tumors, concomitant with a decrease of naïve cells

(**Fig. 3A, Supplementary Fig. S4B**). $CD8^+$ T cells harboring a tissue-resident memory phenotype (TRM $CD8^+$ T) were enriched in infected lungs as compared to the non-infected ones (**Fig. 3B, Supplementary Fig. S4C**). In contrast, no notable changes were observed in the tumor-infiltrating effector $CD4^+$, TRM $CD4^+$ and regulatory $CD4^+$ T cell (Tregs) compartments (**Supplementary Fig. S4D-F**).

We then evaluated the exhaustion state of $CD8^+$ T cells by characterizing the expression of negative immune checkpoints. Unsupervised analysis of the flow cytometry data from tumor-bearing mice with a T-cell marker panel using the Excyted pipeline (https://github.com/maximemeylan/Excyted) (29), which performs automated cell gating and clustering, showed sixteen T-cell clusters (**Fig. 3C**), based on the expression of the markers included in the panel (**Fig. 3D**). In-depth analysis of each cluster showed that five $CD8^+$ T-cells clusters (clusters 2, 3, 6, 12 and 13) were differentially represented in infected and non-infected tumors (**Fig. 3E**). Among them, cluster 12, which was significantly over-represented in IAV-infected tumors, corresponded to exhausted TRM $CD8^+$ T cells expressing PD-1, TIGIT, LAG-3, CD39, CD69 and CD103 (**Fig. 3E**). This result was further confirmed using a classical gating strategy. The expression of PD-1, CTLA-4, TIGIT, LAG-3 or TIM-3 was significantly increased in TRM $CD8^+$ T cells in tumor-bearing lungs following IAV infection, PD-1 being the highest expressed in IAV-infected tumor-bearing and control mice (**Fig. 3F, Supplementary Fig. S4G**). However, IAV did not induce expression of the five immune checkpoints in either the overall $CD8^+$ T-cell compartment (**Supplementary Fig. S4H**) or the non-TRM $CD8^+$ T cells (**Supplementary Fig. S4I**).

Since malignant cells in the KP mice express the SIINFEKL OVA peptide (27), we used specific MHC class I tetramers to analyze the specific T-cell responses against tumor (OVA tetramer) or viral (IAV tetramer) antigens. IAV-specific $CD8^+$ T cells were strongly increased in number in IAV-infected tumors (**Fig. 3G**). In contrast, OVA-specific total $CD8^+$ T cells were diminished in number in infected as compared to non-infected lung tumors (**Fig. 3H**). Furthermore, IAV infection also led to increased PD-1 expression in these OVA tumor-specific $CD8^+$ T cells (from 17% to 32%, P=0.048) (**Fig. 3I**). Importantly, PD-1 expression was significantly higher in tumor-specific than in IAV-specific $CD8^+$ T cells (**Fig. 3J**).

These data show that IAV infection promoted a decrease in the number of tumor-specific $CD8^+$ T cells in the lungs, and that these cells are strongly exhausted, which suggests an impaired anti-tumor response in IAV-infected mice.

IAV induces minor changes in the NK-cell and B-cell compartments and no changes in myeloid cells

Unsupervised analysis of T, NK and B cells from the lungs of KP tumor-bearing mice revealed 18 clusters (**Supplementary Fig. S5A**), which were separated in four groups of cells (B cells, $CD11b^+$ memory B cells, T cells and NK cells), as evidenced by the expression of the markers used in the panel (**Supplementary Fig. S5B**). Four clusters were significantly enriched (T-cell clusters 1 and 2, B-cell cluster 3 and $CD11b^+$ memory B-cell cluster 4) and three excluded (NK-cell cluster 6, B-cell cluster 11, and $CD11b^+$ memory B-cell cluster 13) in tumors of IAV-infected mice as compared to the non-infected ones (**Supplementary Fig. S5C**). Since unsupervised analysis of NK cells and B cells revealed distinct profiles between the different groups of mice, we further examined B-cell subsets by classical flow cytometry evaluation. Viral infection did not modify B-cell compartments based on the expression of IgM and IgD (**Supplementary Fig. S5D**), nor B-cell activation (**Supplementary Fig. S5E**). In addition, no significant impact of viral infection could be observed on myeloid-cell subsets (**Supplementary Fig. S5F**). Altogether, these results show modifications in B-cell and NK-cell clusters.

IAV infection induces a distinct transcriptional profile in tumor-bearing lungs

To decipher the mechanisms involved in the accelerated lung tumor growth we observed upon IAV infection, we analyzed the transcriptional profile of KP tumor-bearing and non-tumor-bearing lungs from IAV-infected and non-infected mice, by RNA-Seq analysis at sacrifice point. The four groups of mice were delineated in four well-defined clusters in a principal component analysis (PCA) (**Fig. 4A**). IAV infection led to the upregulation of 273 genes and downregulation of 12 genes, as represented in the volcano plot (**Fig. 4B**).

Enrichment analyses on the 273 upregulated genes were carried out using Gene Ontology (GO) and KEGG pathways. They revealed enrichment of pathways related to immune response (**Fig. 4C**), anti-viral response, carcinogenesis, lipid metabolism and drug metabolism (**Fig. 4D**). To further annotate

the biological functions enriched in the 273 upregulated genes, we performed gene set enrichment analyses (GSEA). Here again, we observed upregulation of pathways involved in response to viruses (**Fig. 4E**), chemical carcinogenesis (**Fig. 4F**), drug metabolism (**Fig. 4G-J**) and cAMP signaling pathway (**Fig. 4K**). We performed an additional differential gene expression analysis between the four groups of mice by pairwise comparison. The Venn-diagram showed 52 genes (**Supplementary Table S3**) that were specifically overexpressed only in IAV-infected tumors as compared to the other groups (**Fig. 4L**). Altogether, our data show that IAV infection induces a distinct transcriptional signature that distinguishes infected from non-infected tumors. The overexpressed genes are associated with antiviral response, lipid metabolism and drug metabolism, as well as an immune response–related profile.

IAV infection induces a distinct transcriptional profile in *ex vivo* cultures of primary human lung tumors

To characterize the effect of IAV infection in human lung tumors, we infected *ex-vivo* eight primary tumor pieces (7 adenocarcinoma, 1 squamous cell carcinoma) obtained immediately after surgery at the Cochin Hospital (Paris, France) with IAV (MOI around 1). Non-infected tumor pieces served as control. We detected viral infection of tumor cells by HA staining of cytokeratin expressing tumor cells **(Supplementary Fig. S6A)**. We then examined the transcriptional profile by RNA-Seq analysis 24h after infection. We found 27 overexpressed and 17 downregulated genes (log_2 Fold Change>1 and P<0.05) (**Supplementary Fig. S6B, Supplementary Table S4**) associated with immune response processes (**Supplementary Fig. S6C**) and the immune antiviral response (**Supplementary Fig. S6D**). cGMP-PKG, PPAR and Ras signaling pathways, influenza A pathway and TLR signaling pathways were also enriched in KEGG analysis (**Supplementary Fig. S6E**). These results demonstrate that IAV infection modulates the human lung TME, affecting both tumor-associated features (e.g., lipid metabolism and oncogenesis) and the immune response, at early stages of the infection.

The REVISE signature identifies patients with LUAD with poor survival

Because IAV infection induced a specific gene expression signature in lung tumor–bearing mice, we analyzed the cohort of human LUAD patients from TCGA (30) in order to identify such a signature and study its impact on patients' clinical outcome. Of the 273 genes upregulated in the mouse model, we identified 217 human orthologs with expression values in the TCGA dataset. A correlation heatmap of these genes revealed 5 modules, labeled 1 to 5 (**Fig. 5A**, **Table 1**). These subsignatures were identified by a strong internal correlation and by their low correlation between each other. To estimate which cell populations expressed these modules, we analyzed a single-cell RNA-seq dataset of lung adenocarcinoma from GSE131907 (32). We selected only lung tumor samples. Our cell type annotation based on the data provided by the original authors is shown in **Fig. 5B**. We observed the expression pattern of the full signature of 217 genes and of each module (**Fig. 5C-D**). Only module 1 was specific of epithelial cells. We named this gene signature module REVISE (Respiratory Virus Infection Signature in Epithelium, **Table 1**).

We further investigated the clinical relevance of the REVISE signature in human lung adenocarcinoma. Given the distribution of the REVISE expression in the TCGA LUAD cohort, we chose the third quartile as cut-off between high and low expression (**Fig. 5E**). A high expression of the REVISE signature was found to be associated with a poor prognosis in the TCGA LUAD cohort (**Fig. 5F**). To validate this, we obtained data from an independent cohort of human lung adenocarcinoma, OncoSg (31). We similarly separated the cohort into high and low expression of the REVISE signature (**Fig. 5G**) and found that there was a trend towards a significantly worse prognosis for patients with tumors having a high REVISE signature expression (**Fig. 5H**). Finally, to estimate whether the expression of the REVISE signature stems from previous infections of the lung, we analyzed RNA-seq data from large airways epithelium in patients with or without chronic obstructive pulmonary disease (COPD) (**Supplementary Fig. S7**). No significantly different expression of the REVISE signature was observed between patients experiencing COPD and the control cases, which could indicate that the expression of the REVISE signature in the tumor is related to tumor-specific mechanisms and is not due to pre-existing inflammation like COPD.

Discussion

Patients with lung cancer frequently exhibit a compromised immune response that makes them prone to microbial infection. Reciprocally, the consequences of viral infections and the ensuing response on lung cancer progression remains ambiguous. Several studies and clinical case reports have suggested that vaccination against IAV, yellow fever virus and even, SARS-CoV-2, leads to tumor regression (35–37). It has also been shown in murine models, that IAV infection prior to lung tumor initiation enables better control of tumor progression because of the expression of abnormal self-antigens before tumor challenge, which induce immune memory and cancer immunosurveillance (38,39). On the other hand, recent studies have shown that SARS-CoV-2 infection leads to a worse outcome in cancer patients (40), and epidemiological studies evidenced an increased risk of developing lung cancer due to cumulative exposure to IAV (41,42). In line with our observations herein that acute IAV infection leads to tumor progression, Kohlhapp and colleagues demonstrated that lung IAV infection of mice harboring distal melanoma enhances tumor growth and reduces survival (43). We found that tumor cells are infected with IAV and respond with specific transcriptional programs. Indeed, responses to live virus infection and vaccination can be distinct with vaccinations bringing additional adjuvant-induced responses. T cells specific to viral epitopes have also been found in tumors and, upon specific reactivation can lead to tumor growth control by creating an inflammatory environment within the tumor (44). We found that, upon acute IAV infection, the expansion of virus-specific T cells was accompanied by an exhaustion of tumor antigen-specific T cells. Together, the response of tumor cells to virus infection and the expansion of virus-specific T cells to acute IAV infection led to a lower anti-tumor immune response and an increase in tumor growth.

In conclusion, differences observed between studies could be argued due to the different mouse tumor models and viral concentrations used in each of them. In this respect, the KP mouse model used in the present study, harboring $Kras^{G12D}$ mutation with p53 deletion, finely resembles human lung cancer, and IAV infection may mimic its impact on human patients. Additionally, this model is suitable to study the impact of IAV infection, since the Kras mutation itself is unlikely to directly affect the

immune cells in the TME. Indeed, in a previous study, we found no difference in immune cell densities (mature DC and $CD8^+$ T cells) between mutated and wild-type KRAS (10).

Mechanistically, IAV HA protein persisted in malignant cells and in immune cells five weeks post-infection suggesting sustained responses in the TME. IAV considerably impaired tumor-specific T-cell responses. TRM $CD8^+$ T cells were notably increased in the lung tumors following IAV infection, but, crucially, they were exhausted and unable to support an antitumor immune response. IAV infection induced the expression of checkpoint molecules, including PD-1, on tumor-specific TRMs, as well as a strong expression of PD-L1 in the lung epithelial tumor cells. PD-1 expression was significantly higher in tumor-specific TRMs as compared to IAV-specific TRM $CD8^+$ T cells, suggesting that the antigen specificity of the TRMs drove their exhaustion. Echoing our results, Kohlhapp and colleagues showed that upon IAV lung infection, distal melanoma-specific $CD8^+$ T cells migrated to the lungs and expressed high levels of PD-1. Although the main target in their study were not TRM but circulating T cells, PD-1 therapeutic blockade inhibited tumor growth in IAV-infected mice suggesting that PD-1 expression might not be related to TRM cells alone (43). In addition, although to a lesser extent as compared to PD-1, the expression of CTLA-4, TIGIT, LAG-3 and TIM-3 was also stimulated by IAV in our study and their involvement may be interesting to study further in our mouse model. The effect of IAV infection on T-cell exhaustion or T-cell dysfunction has already been described in humans (45) and mice (46) in responses to different viral strains (47) and may be due to the infection of antigen-presenting cells, which impairs their ability to cross-present antigens to $CD8^+$ T cells (48).

Regarding the NK-cell and B-cell compartments, our unsupervised analysis revealed significant differences in seven clusters in the tumors of IAV-infected and non-infected mice. Among them, B-cell and $CD11b^+$ memory B-cell clusters were indistinctly over- and under-represented. The markers included in the panel were not sufficient to more deeply analyze the specific characteristics of each of these clusters. The current study has implications for the evaluation of the B-cell compartment in future studies.

Using RNA sequencing, we identified genes overexpressed in IAV-infected tumor-bearing mice. Strikingly, some of these genes were also up-regulated when primary human lung tumors were infected *ex vivo* with IAV. Despite the different kinetics of the experiments (RNA-Seq experiments were performed 5 weeks and 24h post-infection for *in vivo* mouse models and *ex vivo* primary human tumors, respectively), the induction of *IFIT1*, *OASL* and *DUOXA2* was found in both cases, highlighting their importance in the process from an early time point. These three genes are well-known for their antiviral role against respiratory viruses (49–51), although their implication in lung cancer has not been deeply studied yet. It will be interesting to assess the implication of these genes in lung cancer.

The lack of data on IAV infection experienced by patients from the public cohorts LUAD TCGA and OncoSg cohort prevented us from confirming its direct implication in the accelerated lung tumor progression. However, based on the murine signature, we could translate our data from murine experiments to human. The analysis of differentially expressed genes in the cohort of 273 lung adenocarcinoma patients from the TCGA database revealed a novel signature (REVISE), expressed by epithelial cells, that is likely predictive of an inflammatory gene signature that supports tumor growth, and that could stem from IAV or other previous infections, which may also affect the TME and tumor progression. Of clinical interest, the high expression of the REVISE signature was significantly associated with a poorer overall survival. We propose that the REVISE signature may be used to identify patients with poor clinical outcome.

In summary, our findings indicate a pro-tumoral role of IAV infection in established lung tumors and highlight the impact of the virus on the TME and may explain the epidemiological data showing increased cancer-specific deaths following IAV infection (52).

Author contributions

I. Cremer designed the study. I.G., A.V. and S.M. performed the *in vivo* experiments and analyses. M.A. and N.J. performed the *in vitro* experiments and analyses. A.D.D. and O.L. generated the KP lung tumor-bearing mice. M.M. designed the Excyted pipeline for unsupervised flow cytometry analyses. D.D., A.L.P. and M.A. collected human tumor specimens. I.G.V. and J.M.S. prepared and provided IAV. L.M. established the KP cell line. I.M., S.M., P.E.F., and F.P. performed bioinformatic analyses. I.G., A.V. and S.M. generated the figures and tables. I.G. and I.C. wrote the manuscript. All authors discussed the results and commented on the manuscript.

Acknowledgements

We thank the Cochin hospital for contributing to the tissue collection. We also thank the CHIC (Center of Histology Imaging and Cytometry) and the CEF (Center for animal experiment) facilities of the Centre de Recherche des Cordeliers.

This work was supported by the “Institut National de la Sante et de la Recherche Medicale” (INSERM), Sorbonne Universite, Universite de Paris, the LabEx Immuno-Oncology, the Institut National du Cancer (2016-PLBIO) and foundation ARC.

References

1. Gentles AJ, Newman AM, Liu CL, Bratman SV, Feng W, Kim D, et al. The prognostic landscape of genes and infiltrating immune cells across human cancers. Nat Med. 2015;21(8):938–45.

2. Damotte D, Warren S, Arrondeau J, Boudou-Rouquette P, Mansuet-Lupo A, Biton J, et al. The tumor inflammation signature (TIS) is associated with anti-PD-1 treatment benefit in the CERTIM pan-cancer cohort. J Transl Med. 2019;17(1):357.

3. Petitprez F, Meylan M, de Reyniès A, Sautès-Fridman C, Fridman WH. The Tumor Microenvironment in the Response to Immune Checkpoint Blockade Therapies. Front Immunol. 2020;11:784.

4. Altorki NK, Markowitz GJ, Gao D, Port JL, Saxena A, Stiles B, et al. The lung microenvironment: an important regulator of tumour growth and metastasis. Nat Rev Cancer. 2019;19(1):9–31.

5. Germain C, Gnjatic S, Tamzalit F, Knockaert S, Remark R, Goc J, et al. Presence of B cells in tertiary lymphoid structures is associated with a protective immunity in patients with lung cancer. Am J Respir Crit Care Med. 2014;189(7):832–44.

6. de Chaisemartin L, Goc J, Damotte D, Validire P, Magdeleinat P, Alifano M, et al. Characterization of chemokines and adhesion molecules associated with T cell presence in tertiary lymphoid structures in human lung cancer. Cancer Res. 2011;71(20):6391–9.

7. Platonova S, Cherfils-Vicini J, Damotte D, Crozet L, Vieillard V, Validire P, et al. Profound coordinated alterations of intratumoral NK cell phenotype and function in lung carcinoma. Cancer Res. 2011;71(16):5412–22.

8. Lavin Y, Kobayashi S, Leader A, Amir EAD, Elefant N, Bigenwald C, et al. Innate Immune Landscape in Early Lung Adenocarcinoma by Paired Single-Cell Analyses. Cell. 2017;169(4):750-765.e17.

9. Russick J, Joubert PE, Gillard-Bocquet M, Torset C, Meylan M, Petitprez F, et al. Natural killer cells in the human lung tumor microenvironment display immune inhibitory functions. J Immunother Cancer. 2020;8(2):e001054.

10. Mansuet-Lupo A, Alifano M, Pécuchet N, Biton J, Becht E, Goc J, et al. Intratumoral Immune Cell Densities Are Associated with Lung Adenocarcinoma Gene Alterations. Am J Respir Crit Care Med. 2016;194(11):1403–12.

11. Biton J, Mansuet-Lupo A, Pécuchet N, Alifano M, Ouakrim H, Arrondeau J, et al. TP53, STK11, and EGFR Mutations Predict Tumor Immune Profile and the Response to Anti-PD-1 in Lung Adenocarcinoma. Clin Cancer Res. 2018;24(22):5710–23.

12. Hua X, Zhao W, Pesatori AC, Consonni D, Caporaso NE, Zhang T, et al. Genetic and epigenetic intratumor heterogeneity impacts prognosis of lung adenocarcinoma. Nat Commun. 2020;11(1):2459.

13. Vanhove K, Graulus GJ, Mesotten L, Thomeer M, Derveaux E, Noben JP, et al. The Metabolic Landscape of Lung Cancer: New Insights in a Disturbed Glucose Metabolism. Front Oncol. 2019;9:1215.

14. Ramírez-Labrada AG, Isla D, Artal A, Arias M, Rezusta A, Pardo J, et al. The Influence of Lung Microbiota on Lung Carcinogenesis, Immunity, and Immunotherapy. Trends Cancer. 2020;6(2):86–97.

15. Jin C, Lagoudas GK, Zhao C, Bullman S, Bhutkar A, Hu B, et al. Commensal Microbiota Promote Lung Cancer Development via γδ T Cells. Cell. 2019;176(5):998-1013.e16.

16. Tsay JCJ, Wu BG, Badri MH, Clemente JC, Shen N, Meyn P, et al. Airway Microbiota Is Associated with Upregulation of the PI3K Pathway in Lung Cancer. Am J Respir Crit Care Med. 2018;198(9):1188–98.

17. Tsay JCJ, Wu BG, Sulaiman I, Gershner K, Schluger R, Li Y, et al. Lower Airway Dysbiosis Affects Lung Cancer Progression. Cancer Discov. 2021;11(2):293–307.

18. Iuliano AD, Roguski KM, Chang HH, Muscatello DJ, Palekar R, Tempia S, et al. Estimates of global seasonal influenza-associated respiratory mortality: a modelling study. Lancet. 2018;391(10127):1285–300.

19. Angrini M, Varthaman A, Garcia-Verdugo I, Sallenave JM, Alifano M, Cremer I. To Vaccinate or not: Influenza Virus and Lung Cancer Progression. Trends Cancer. 2021;7:573–6.

20. Kinslow CJ, Wang Y, Liu Y, Zuev KM, Wang TJC, Donalek CM, et al. Influenza and mortality for non-small cell lung cancer. JCO. 2019;37(15_suppl):e13114–e13114.

21. Kunisaki KM, Janoff EN. Influenza in immunosuppressed populations: a review of infection frequency, morbidity, mortality, and vaccine responses. Lancet Infect Dis. 2009;9(8):493–504.

22. Pang IK, Pillai PS, Iwasaki A. Efficient influenza A virus replication in the respiratory tract requires signals from TLR7 and RIG-I. Proc Natl Acad Sci U S A. 2013;110(34):13910–5.

23. Chatterjee S, Crozet L, Damotte D, Iribarren K, Schramm C, Alifano M, et al. TLR7 promotes tumor progression, chemotherapy resistance, and poor clinical outcomes in non-small cell lung cancer. Cancer Res. 2014;74(18):5008–18.

24. Cherfils-Vicini J, Platonova S, Gillard M, Laurans L, Validire P, Caliandro R, et al. Triggering of TLR7 and TLR8 expressed by human lung cancer cells induces cell survival and chemoresistance. J Clin Invest. 2010;120(4):1285–97.

25. Dajon M, Iribarren K, Petitprez F, Marmier S, Lupo A, Gillard M, et al. Toll like receptor 7 expressed by malignant cells promotes tumor progression and metastasis through the recruitment of myeloid derived suppressor cells. Oncoimmunology. 2019;8(1):e1505174.

26. DuPage M, Dooley AL, Jacks T. Conditional mouse lung cancer models using adenoviral or lentiviral delivery of Cre recombinase. Nat Protoc. 2009;4(7):1064–72.

27. Alonso R, Flament H, Lemoine S, Sedlik C, Bottasso E, Péguillet I, et al. Induction of anergic or regulatory tumor-specific CD4+ T cells in the tumor-draining lymph node. Nat Commun. 2018;9(1):2113.

28. Sanchez-Guzman D, Le Guen P, Villeret B, Sola N, Le Borgne R, Guyard A, et al. Silver nanoparticle-adjuvanted vaccine protects against lethal influenza infection through inducing BALT and IgA-mediated mucosal immunity. Biomaterials. 2019;217:119308.

29. Meylan M. Excyted pipeline. https://github.com/maximemeylan/Excyted. https://github.com/maximemeylan/Excyted; 2021.

30. Cancer Genome Atlas Research Network. Comprehensive molecular profiling of lung adenocarcinoma. Nature. 2014;511(7511):543–50.

31. Chen J, Yang H, Teo ASM, Amer LB, Sherbaf FG, Tan CQ, et al. Genomic landscape of lung

adenocarcinoma in East Asians. Nat Genet. 2020;52(2):177–86.

32. Kim N, Kim HK, Lee K, Hong Y, Cho JH, Choi JW, et al. Single-cell RNA sequencing demonstrates the molecular and cellular reprogramming of metastatic lung adenocarcinoma. Nat Commun. 2020;11(1):2285.

33. Hao Y, Hao S, Andersen-Nissen E, Mauck WM, Zheng S, Butler A, et al. Integrated analysis of multimodal single-cell data. Cell. 2021;184(13):3573-3587.e29.

34. Morrow JD, Chase RP, Parker MM, Glass K, Seo M, Divo M, et al. RNA-sequencing across three matched tissues reveals shared and tissue-specific gene expression and pathway signatures of COPD. Respir Res. 2019;20(1):65.

35. Aznar MA, Molina C, Teijeira A, Rodriguez I, Azpilikueta A, Garasa S, et al. Repurposing the yellow fever vaccine for intratumoral immunotherapy. EMBO Mol Med. 2020;12(1):e10375.

36. Sousa LG de, McGrail DJ, Li K, Marques-Piubelli ML, Gonzalez C, Dai H, et al. Spontaneous tumor regression following COVID-19 vaccination. J Immunother Cancer. 2022;10(3):e004371.

37. Newman JH, Chesson CB, Herzog NL, Bommareddy PK, Aspromonte SM, Pepe R, et al. Intratumoral injection of the seasonal flu shot converts immunologically cold tumors to hot and serves as an immunotherapy for cancer. Proc Natl Acad Sci. 2020;117(2):1119–28.

38. Masemann D, Köther K, Kuhlencord M, Varga G, Roth J, Lichty BD, et al. Oncolytic influenza virus infection restores immunocompetence of lung tumor-associated alveolar macrophages. Oncoimmunology. 2018;7(5):e1423171.

39. Iheagwara UK, Beatty PL, Van PT, Ross TM, Minden JS, Finn OJ. Influenza virus infection elicits protective antibodies and T cells specific for host cell antigens also expressed as tumor-associated antigens: a new view of cancer immunosurveillance. Cancer Immunol Res. 2014;2(3):263–73.

40. De Winter FHR, Hotterbeekx A, Huizing MT, Konnova A, Fransen E, Jongers B, et al. Blood Cytokine Analysis Suggests That SARS-CoV-2 Infection Results in a Sustained Tumour Promoting Environment in Cancer Patients. Cancers (Basel). 2021;13(22):5718.

41. Inaida S, Matsuno S. Previous Infection Positively Correlates to the Tumor Incidence Rate of

Patients with Cancer. Cancer Immunol Res. 2020;8(5):580–6.

42. Weng CF, Chen LJ, Lin CW, Chen HM, Lee HHC, Ling TY, et al. Association between the risk of lung cancer and influenza: A population-based nested case-control study. Int J Infect Dis. 2019;88:8–13.

43. Kohlhapp FJ, Huelsmann EJ, Lacek AT, Schenkel JM, Lusciks J, Broucek JR, et al. Non-oncogenic acute viral infections disrupt anti-cancer responses and lead to accelerated cancer-specific host death. Cell Rep. 2016;17(4):957–65.

44. Rosato PC, Wijeyesinghe S, Stolley JM, Nelson CE, Davis RL, Manlove LS, et al. Virus-specific memory T cells populate tumors and can be repurposed for tumor immunotherapy. Nat Commun. 2019;10(1):567.

45. Liu S, Huang Z, Fan R, Jia J, Deng X, Zou X, et al. Cycling and activated CD8+ T lymphocytes and their association with disease severity in influenza patients. BMC Immunol. 2022;23(1):40.

46. Erickson JJ, Gilchuk P, Hastings AK, Tollefson SJ, Johnson M, Downing MB, et al. Viral acute lower respiratory infections impair CD8+ T cells through PD-1. J Clin Invest. 2012;122(8):2967–82.

47. Ou H, Chen L, Wu H. Enhanced Programmed Cell Death Protein 1/Programmed Cell Death Ligand 1 Expression Induced by Severe Influenza A Virus Infection Impairs Host's Antiviral Response. Viral Immunol. 2022;35(8):566–76.

48. Smed-Sörensen A, Chalouni C, Chatterjee B, Cohn L, Blattmann P, Nakamura N, et al. Influenza A virus infection of human primary dendritic cells impairs their ability to cross-present antigen to CD8 T cells. PLoS Pathog. 2012;8(3):e1002572.

49. Zhao L, Xia M, Wang K, Lai C, Fan H, Gu H, et al. A Long Non-coding RNA IVRPIE Promotes Host Antiviral Immune Responses Through Regulating Interferon β1 and ISG Expression. Front Microbiol. 2020;11:260.

50. Zhu J, Zhang Y, Ghosh A, Cuevas RA, Forero A, Dhar J, et al. Antiviral activity of human OASL protein is mediated by enhancing signaling of the RIG-I RNA sensor. Immunity. 2014;40(6):936–48.

51. Grasberger H, Refetoff S. Identification of the maturation factor for dual oxidase. Evolution of

an eukaryotic operon equivalent. J Biol Chem. 2006;281(27):18269–72.

52. Li J, Zhang D, Sun Z, Bai C, Zhao L. Influenza in hospitalised patients with malignancy: a propensity score matching analysis. ESMO Open. 2020;5(5):e000968.

Table 1. Genes included in REVISE signature defined in the cohort of LUAD patients from TCGA.

REVISE signature
MSLN
ERN2
FXYD3
PLA2G10
AGR2
FAM83E
ENTPD8
SPINK4
KCNE3
MISP
SDCBP2
TFF1
GCNT3
FA2H
BCAS1
CDHR5
TM4SF5
ANKS4B
HNF4A
EPS8L3
ONECUT2
KRT20
HNF4G
C2orf72
VIL1
CDH17
ANXA13
BAIAP2L2
SMIM24
HSD17B2
LGALS4
CYP3A5
TM4SF4
DUOX2
DUOXA2
SMPD3
IHH
ALDOB
NR1I2
ANXA10
MYO1A
FER1L6
UGT2A3
TFF2
REG4
PSCA
ARL14
SULT1B1
PTPRR
CYP3A4
REP15

Figures

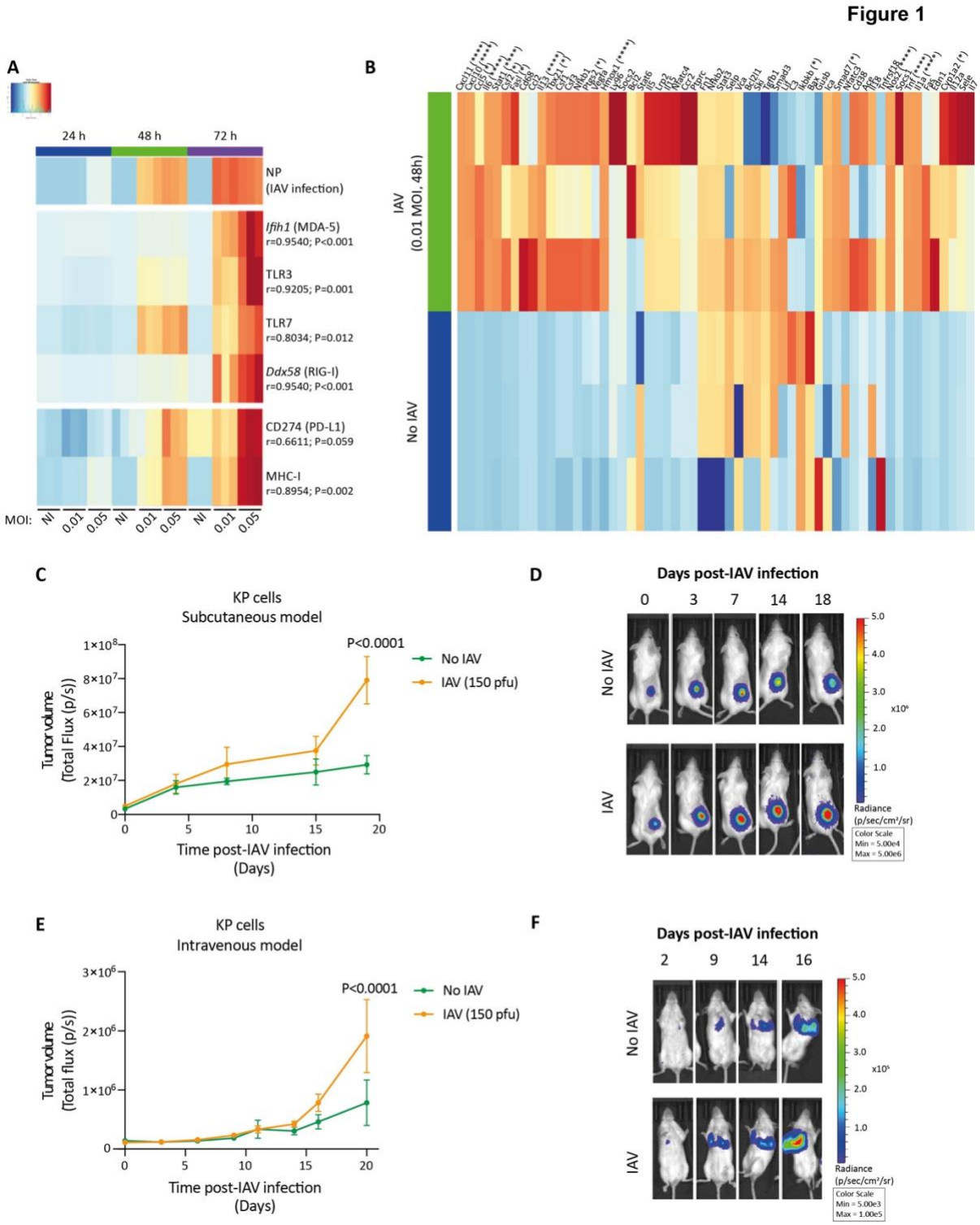

Fig. 1. IAV infection enhances tumor growth in KP cells-injected subcutaneous and orthotopic models. A. Heatmaps showing percentage of IAV-infected KP cells, viral sensor expression and PD-L1 and MHC-I expression in non-infected (NI) and IAV-infected (0.01 and 0.05 MOI) KP cells 24, 48 and 72

hours post-infection. IAV infection was assessed by flow cytometry using anti-NP. mRNA expression of viral sensors (MDA-5, TLR3, TLR7, RIG-I) was analyzed by RT-qPCR and fold change comparing infected- and non-infected cells is shown. *Gapdh* was used as control gene. PD-L1 and MHC-I expression were analyzed by flow cytometry, and data are shown as Mean Fluorescent Intensity represented as fold change comparing infected- and non-infected cells. Correlation between IAV infection and the expression of viral sensors, PD-L1 and MHC-I was calculated by Spearman correlation. For each correlation, r and P values are indicated. **B.** Heatmap representing expression of cytokines and chemokines as studied by RT-qPCR with the TaqMan Array Mouse Immune Panel in non-infected and IAV-infected KP cells (0.01 MOI) after 48 hours infection. Data are shown as fold change comparing infected- and non-infected cells and differences between groups were analyzed by linear regression with Benjamini-Hochberg correction for multiple testing. *Gapdh* was used as housekeeping gene. All experiments were repeated at least three times. **C.** Intratumoral IAV infection (150 pfu/mice) was performed in mice subcutaneously injected with KP cells 13 days prior to the IAV infection. Tumor burden was followed up by bioluminescence. IAV significantly enhanced tumor growth as compared to PBS-treated mice. Total flux differences among groups were compared using the 2-way ANOVA test (n=5 mice per group). Error bars: mean ± standard deviation. **D.** Representative images of bioluminescence IVIS acquisition (of the Figure 1C) in subcutaneous tumor-bearing mice at days 0, 3, 7, 14 and 18 post-IAV infection. **E.** Mice intravenously injected with KP cells were intranasally inoculated with 150 pfu/mice IAV when tumors were detectable (total flux around $1x10^5$ photon/s, around day 13 post- cell injection). Tumor burden was followed up by bioluminescence. IAV significantly enhanced tumor growth as compared to non-infected mice. Total flux differences among groups were compared using the 2-way ANOVA test (n=9 mice per group). Error bars: mean ± standard deviation. **F.** Representative images of bioluminescence IVIS acquisition (of the Figure 1E) in intravenously injected tumor-bearing mice at days 2, 9, 14 and 16 post-IAV infection. *P<0.05, **P<0.01, ***P<0.001, ****P<0.0001.

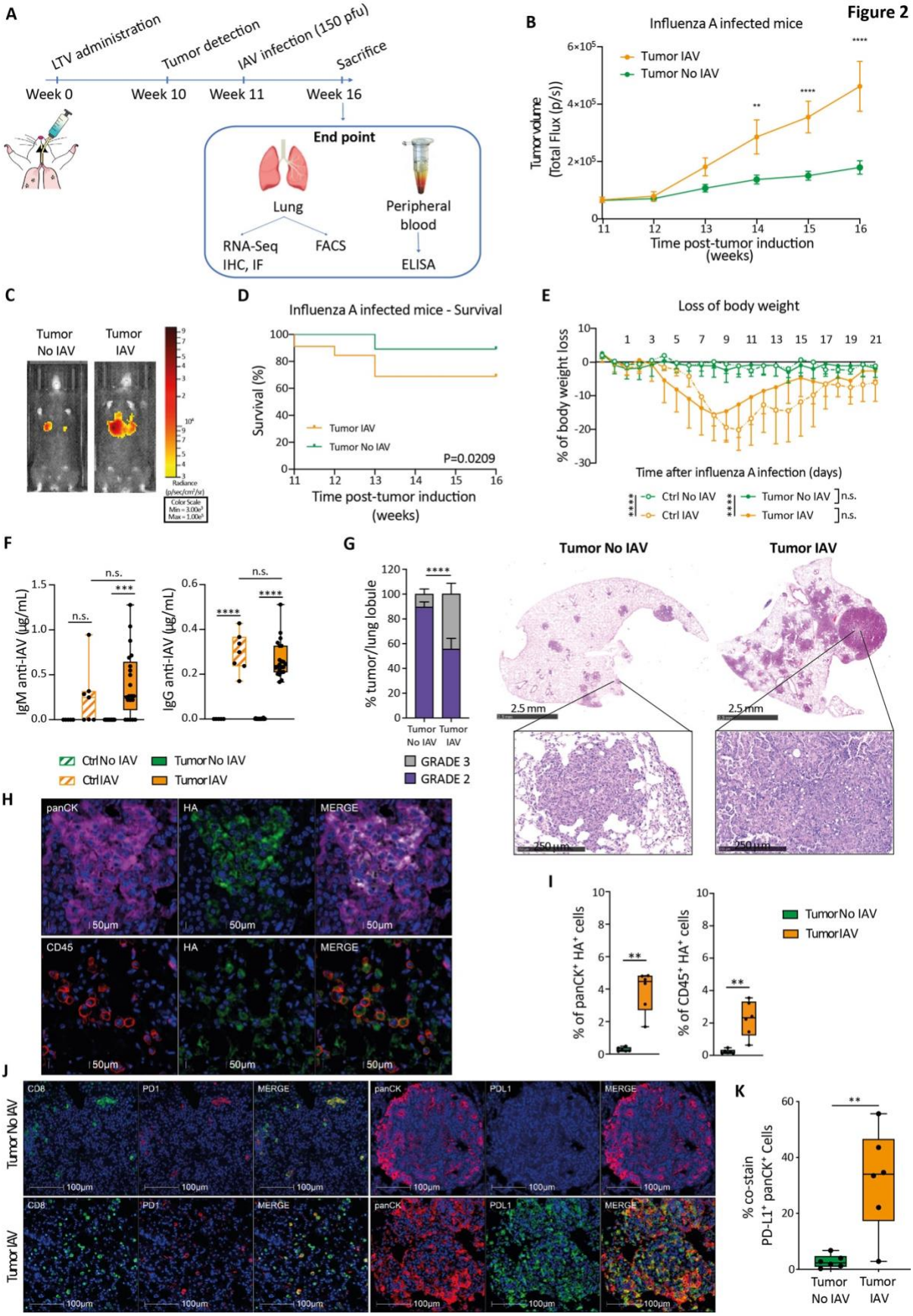
A
LTV administration
Tumor detection
IAV infection (150 pfu)
Sacrifice
Week 0
Week 10
Week 11
Week 16
End point
Lung
Peripheral blood
RNA-Seq
IHC, IF
FACS
ELISA
B
Influenza A infected mice
Tumor IAV
Tumor No IAV
Tumor volume (Total Flux (p/s))
Time post-tumor induction (weeks)
C
Tumor No IAV
Tumor IAV
D
Influenza A infected mice - Survival
Survival (%)
P=0.0209
Time post-tumor induction (weeks)
E
Loss of body weight
% of body weight loss
Time after influenza A infection (days)
Ctrl No IAV
Ctrl IAV
Tumor No IAV
Tumor IAV
n.s.
F
IgM anti-IAV (µg/mL)
IgG anti-IAV (µg/mL)
n.s.
Ctrl No IAV
Ctrl IAV
Tumor No IAV
Tumor IAV
G
% tumor/lung lobule
Tumor No IAV
Tumor IAV
GRADE 3
GRADE 2
Tumor No IAV
Tumor IAV
2.5 mm
250µm
H
panCK
HA
MERGE
CD45
50µm
I
% of panCK+ HA+ cells
% of CD45+ HA+ cells
Tumor No IAV
Tumor IAV
J
CD8
PD1
MERGE
panCK
PDL1
Tumor No IAV
Tumor IAV
100µm
K
% co-stain PD-L1+ panCK+ Cells
Tumor No IAV
Tumor IAV

Fig. 2. Intranasal infection by IAV in tumor-bearing lungs significantly enhances tumor growth with higher grade nodules in KP mice. A. Diagram of experimental workflow. Three independent experiments were performed. **B**. Tumor growth in the lungs of KP mice with a single dose of IAV (week 11). Total flux differences among groups were analyzed at each time-point using the 2-way ANOVA test (n≥31 mice per group). Error bars: mean ± standard deviation. **C.** Representative images of bioluminescence IVIS acquisition in tumor-bearing mice 5 weeks post-infection. **D.** Survival curves of non-infected and IAV infected tumor-bearing mice. p-value was determined by the logrank test. **E.** Percentage of mice body weight loss was measured in the following days of IAV infection. Differences among groups were analyzed at each time-point with the 2-way ANOVA test. Error bars: mean ± standard deviation. **F.** Circulating anti-IAV IgM (**left panel**) and IgG (**right panel**) antibodies were measured by ELISA in non-infected and infected mice at sacrifice point. Error bars: median ± interquartile range and groups compared by one-way ANOVA test (n≥5). **G. Left:** percentage of number of tumor nodules with grade 2 and 3 per total lung lobule in tumor-harboring lungs. Groups were compared with the Chi-Squared test (n≥7). Error bars: mean ± standard deviation. **Right:** representative histological images of tumors with grade 2 and 3 in the lungs of non-infected and IAV-infected KP mice 5 weeks post-infection. Scale bars: 2.5 mm and 250 µm. **H.** Representative images of multiplex immunofluorescence for panCK (magenta), CD45 (red) and HA (green) in tumor-bearing mice. DAPI staining is shown in blue. Scale bar: 50 µm. HA: Hemagglutinin protein expressed on the surface of IAV. **I.** Percentage of $panCK^+HA^+$ tumor cells (**left panel**) and $CD45^+HA^+$ immune cells (**right panel**) in non-infected or IAV-infected mice. Error bars: median ± interquartile range (n=6). Groups were compared by using the Mann-Whitney *U* test. **J.** Representative immunofluorescence staining of lung tumors from non-infected and IAV-infected mice for CD8 (green), PD-1 (red), panCK (red) and PD-L1 (green). DAPI staining is shown in blue. Scale bar: 100 µm. **K.** Percentages of cells positive for PD-L1 and panCK double staining in non-infected and IAV-infected tumor-bearing lungs. Quantification of the staining was performed on entire slides. Error bars: median ± interquartile range (n=6 for both groups)

and differences among groups were studied by the Mann-Whitney *U* test. *P<0.05, **P<0.01, ***P<0.001, ****P<0.0001, n.s. = non-significant.

Figure 3

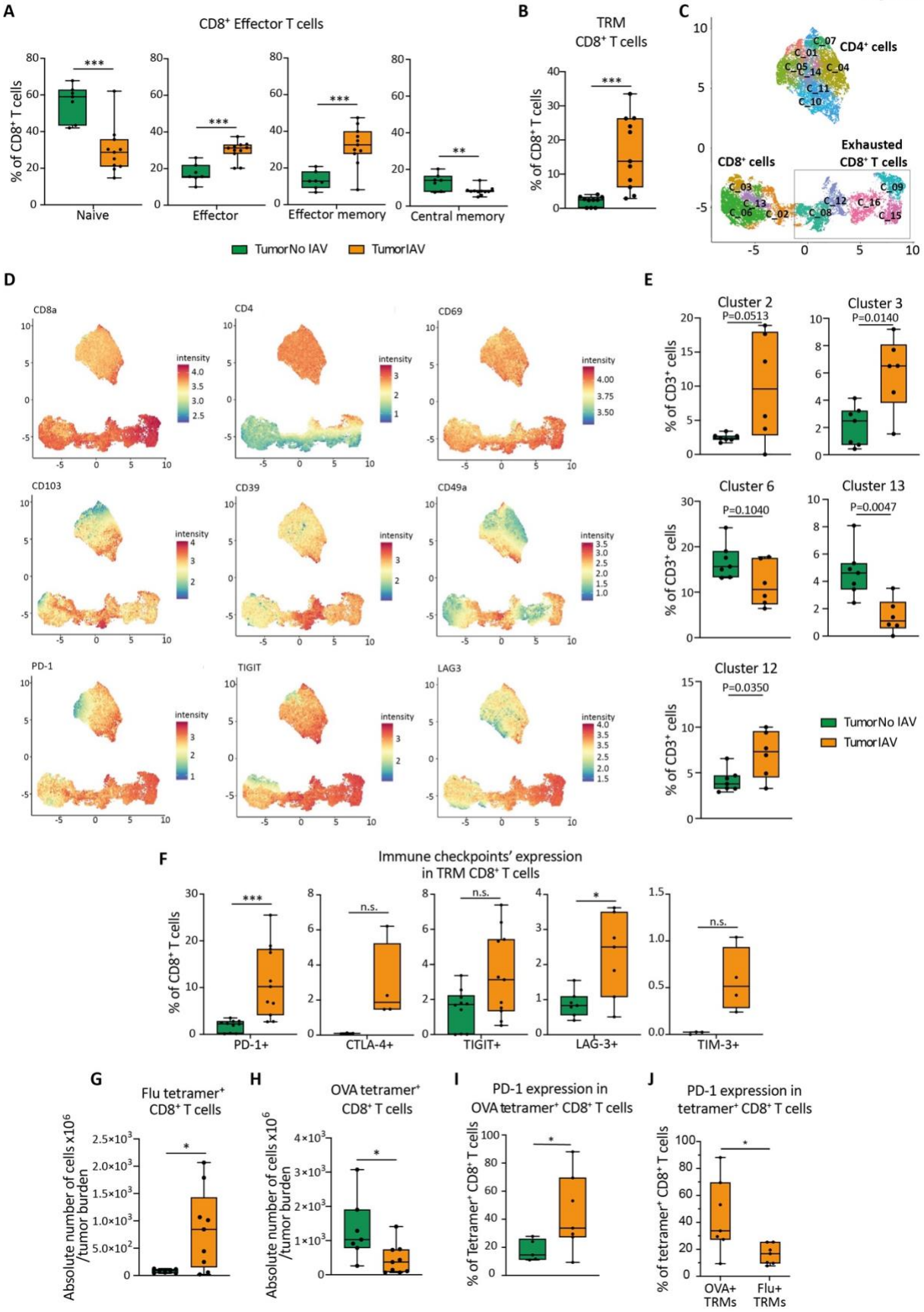
A
CD8⁺ Effector T cells
% of CD8⁺ T cells
Naive
Effector
Effector memory
Central memory
Tumor No IAV
Tumor IAV
B
TRM CD8⁺ T cells
C
CD4⁺ cells
CD8⁺ cells
Exhausted CD8⁺ T cells
D
CD8a
CD4
CD69
CD103
CD39
CD49a
PD-1
TIGIT
LAG3
intensity
E
Cluster 2
P=0.0513
Cluster 3
P=0.0140
Cluster 6
P=0.1040
Cluster 13
P=0.0047
Cluster 12
P=0.0350
% of CD3⁺ cells
F
Immune checkpoints' expression in TRM CD8⁺ T cells
PD-1+
CTLA-4+
TIGIT+
LAG-3+
TIM-3+
n.s.
G
Flu tetramer⁺ CD8⁺ T cells
Absolute number of cells x10⁶ /tumor burden
H
OVA tetramer⁺ CD8⁺ T cells
I
PD-1 expression in OVA tetramer⁺ CD8⁺ T cells
% of Tetramer⁺ CD8⁺ T cells
J
PD-1 expression in tetramer⁺ CD8⁺ T cells
% of tetramer⁺ CD8⁺ T cells
OVA+ TRMs
Flu+ TRMs

Fig. 3. Intratumoral T-cell compartment is significantly affected by IAV infection. Flow cytometry was performed on cells isolated from the lungs of KP mice. **A.** Percentages of naïve ($CD44^{-}CD62L^{+}$), effector ($CD44^{-}CD62L^{-}$), effector memory ($CD44^{+}CD62L^{-}$) and central memory ($CD44^{+}CD62L^{+}$) $CD8^{+}$ T cells in tumor-bearing mice (n≥7 for all groups). **B.** Percentages of $CD8^{+}$ T cells with a tissue-resident memory phenotype (TRM). TRM $CD8^{+}$ T-cell population was selected as CD103, CD69, CD49a and CD39 expressing cells. The presence of TRM $CD8^{+}$ T cells was significantly increased in IAV-infected tumor-bearing lungs as compared to non-infected tumors (n≥10 for both groups). Error bars in graphs **A-B:** median ± interquartile range. Differences between groups were studied by multiple Mann-Whitney tests with Benjamini-Hochberg correction. **C.** Umap analysis of T cells in IAV-infected and non-infected tumor-bearing mice classified the cells in 16 different clusters. **D.** Relative expression of each individual marker from the panel is shown for all the clusters in the Umap. **E.** Clusters 2, 3 and 12 were markedly over-represented and clusters 6 and 13 were excluded in IAV-infected tumor-bearing lungs as compared to the non-infected ones. Error bars: median ± interquartile range (n≥6 for both groups). Comparison among groups was performed by the Mann-Whitney *U* test. **F.** Percentages of immune checkpoint–expressing TRM $CD8^{+}$ T cells in tumor-bearing mice. **G.** Absolute number of OVA $tetramer^{+}$ $CD8^{+}$ T cells per tumor size in non-infected and infected tumor-bearing mice (n≥7 for both groups). **H.** Absolute number of IAV $tetramer^{+}$ $CD8^{+}$ T cells in mice bearing KP tumors (n≥7 for both groups). **I.** Percentages of PD-1–expressing OVA-$tetramer^{+}$ $CD8^{+}$ T cells in tumors (n≥6). Error bars in graphs **F-I**: median ± interquartile range. Comparisons among groups were performed by Benjamini-Hochberg correction of multiple Mann-Whitney tests. **J.** Percentages of PD-1 expressing OVA-$tetramer^{+}$ and IAV-$tetramer^{+}$ $CD8^{+}$ T cells in IAV-infected tumor-bearing mice. Error bar: median ± interquartile range. Groups were compared with the Mann-Whitney *U* test (n=7 for both groups). *P<0.05, **P<0.01, ***P<0.001.

Figure 4

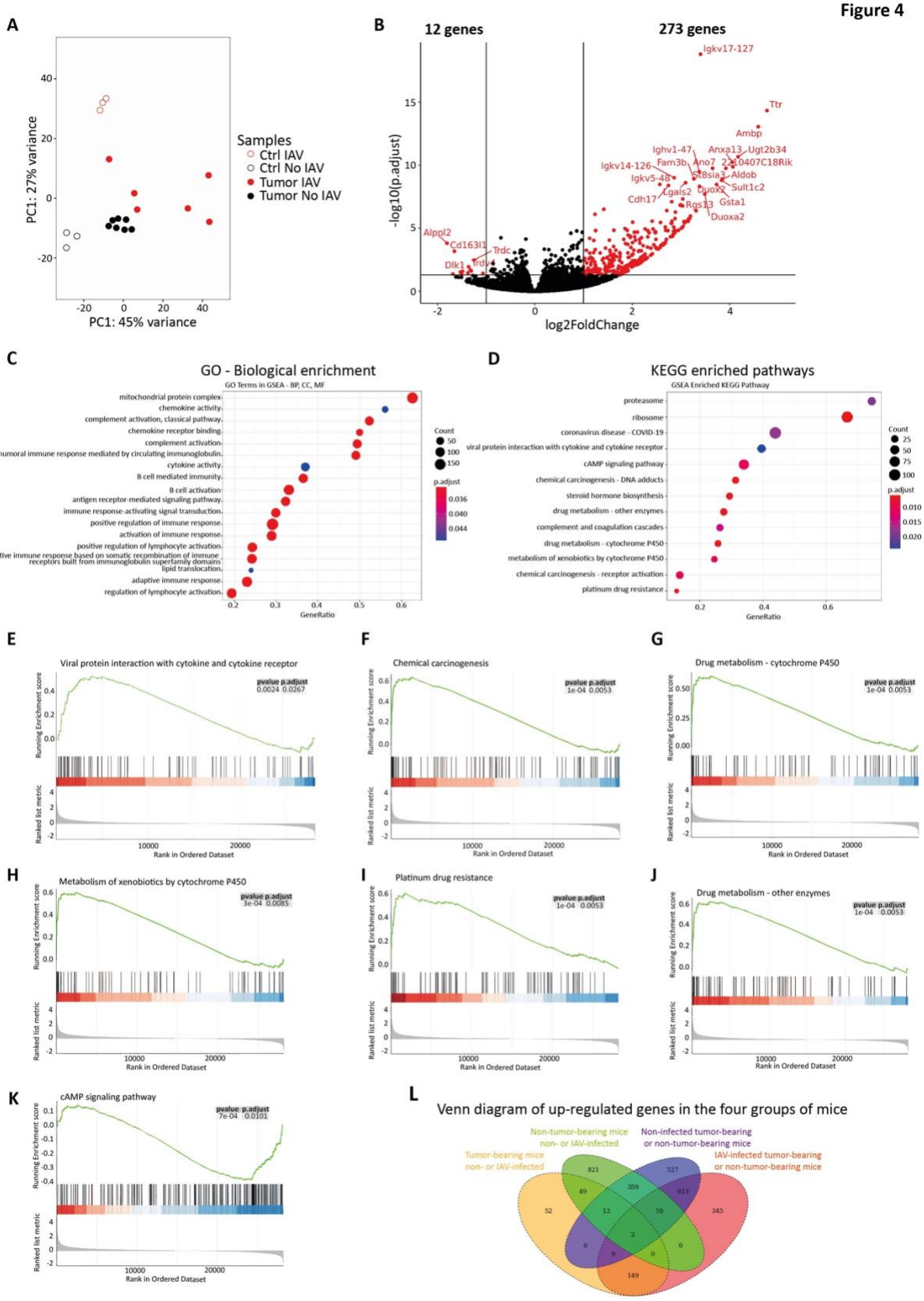

Fig. 4. Analysis of differentially expressed genes reveals a distinct transcriptional profile that distinguishes IAV-infected tumor-bearing KP mice from non-infected tumor-bearing ones. A.

Principal component analysis of the mRNA expression values of samples from the four groups of mice, based on their normalized scores. PC1 (horizontal axis) accounted for 45%, while PC2 (vertical axis) accounted for 27% of the observed variation. **B.** Volcano plot showing differentially expressed genes between IAV-infected tumor-bearing lungs and non-infected tumors. Red dots in the right side represent upregulated genes (n=273) and red dots in the left side represent downregulated genes (n=12) in infected tumors. Differentially expressed genes screening cutoff: $\log_2$ Fold Change>1 and P<0.05. **C.** Pathway enrichment Gene Ontology (GO) analysis of upregulated genes in IAV-infected tumor-bearing mice (FDR<0.05 and P<0.05). Y-axis indicates the enriched GO terms; X-axis represents the number of genes in each GO term. **D.** KEGG pathway analysis of the up-regulated genes. X-axis represents gene ratio (number of genes participating in the pathway in this study/number of total genes that participate in this pathway). Color and size of the dots correspond to enrichment significance and amount of input genes enriched in the pathway, respectively. **E-K.** Enrichment plots of gene expression signatures were analyzed by GSEA. **L.** Venn diagram illustrating the number of up-regulated genes in the four groups of mice revealed by pairwise comparisons as performed by DESeq2 gene expression analysis (FDR ≥ 0.01, adjusted P-value < 0.05) between tumor-bearing mice infected or not with IAV (yellow, 273 genes), control mice infected or not with IAV (green, 1293 genes), uninfected tumor-bearing or control mice (blue, 1572 genes), and IAV-infected tumor-bearing or control mice (red, 1168 genes).

Figure 5

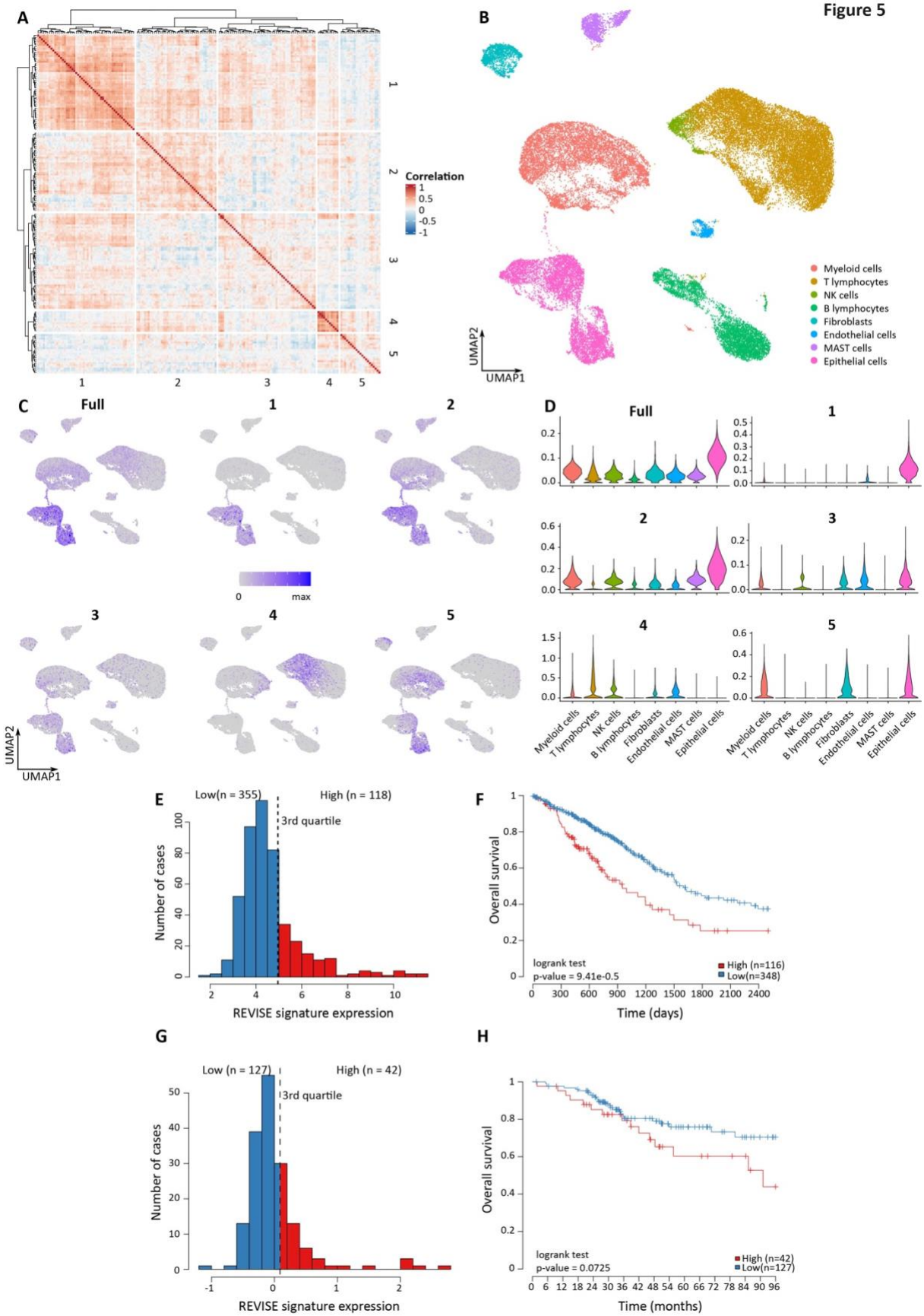
A
Correlation
1
0.5
0
-0.5
-1
B
Myeloid cells
T lymphocytes
NK cells
B lymphocytes
Fibroblasts
Endothelial cells
MAST cells
Epithelial cells
UMAP2
UMAP1
C
Full
1
2
3
4
5
0
max
D
Full
1
2
3
4
5
Myeloid cells
T lymphocytes
NK cells
B lymphocytes
Fibroblasts
Endothelial cells
MAST cells
Epithelial cells
E
Low(n = 355)
High (n = 118)
3rd quartile
Number of cases
REVISE signature expression
F
Overall survival
logrank test
p-value = 9.41e-0.5
High (n=116)
Low(n=348)
Time (days)
G
Low (n = 127)
High (n = 42)
3rd quartile
Number of cases
REVISE signature expression
H
Overall survival
logrank test
p-value = 0.0725
High (n=42)
Low(n=127)
Time (months)

Fig. 5. The epithelial module of genes upregulated upon flu infection predicts a poor prognosis in human lung adenocarcinoma patients. A. Correlation of the expression of gene orthologs for genes upregulated in flu-infected mice tumors, in the TCGA LUAD cohort. The hierarchical clustering shows 5 modules, labeled 1 to 5. **B.** UMAP of the single cell RNA-seq atlas of human lung adenocarcinoma (from cohort GSE131907) colored by cell type. **C.** Mapping of the expression of the full gene signature or its modules 1-5 on the UMAP defined on panel B. The module labels correspond to the ones defined on panel A. **D.** Violin plot showing the expression of the full gene signature and its modules in the various cell types. Module 1 is specific to epithelial cells and henceforth called REVISE (Respiratory Virus Infection in Epithelium). **E.** Distribution of the expression of the REVISE signature in the TCGA LUAD cohort. The cut-off between High and Low expression is based on the third quartile. **F.** Kaplan-Meier overall survival curves of the TCGA LUAD cohort based on the expression of REVISE gene signature. Significance was established using a log-rank test. **G.** Distribution of the expression of the REVISE signature in the OncoSg cohort. The cut-off between High and Low expression is based on the third quartile. **H.** Kaplan-Meier survival overall survival curves of the OncoSg cohort based on the expression of the REVISE gene signature.